IOP Publishing | Bureau International des Poids et Mesures Metrologia

Metrologia **61** (2024) 065004 (16pp) https://doi.org/10.1088/1681-7575/ad77db

Conversion of a piston–cylinder dimensional dataset to the effective area of a mechanical pressure generator

Patrick F Egan*, Eric S Stanfield, John R Stoup and Christopher W Meyer

National Institute of Standards and Technology, 100 Bureau Dr, Gaithersburg, MD 20899, United States of America

E-mail: egan@nist.gov

Received 19 July 2024, revised 4 September 2024
Accepted for publication 6 September 2024
Published 7 October 2024

Abstract

Recent developments in diameter metrology at NIST have improved the dimensional characterization of piston–cylinder assemblies (PCAs) to unprecedented precision. For the newest generation of PCAs, the standard uncertainty in the measurement of the outer diameter is 12 nm, while uncertainty in the measurement of the inner diameter is 14 nm. With a high-accuracy dimensional dataset in hand, the task of determining the pressure generated by a specific PCA is reduced to converting the diameter (and straightness and roundness) to an effective area (and distortion coefficient). The details on how this was performed for the artifact PCA2062 are described. PCA2062 was dimensioned in 2017 and 2020; the area repeated within $0.2 \times 10^{-6} \cdot A_0$. The calculation produced estimates of fall rate and rotation decay that agreed with experimental observations within 12 %. The fall rate is proportional to the square of the gap width; therefore, the agreement between calculation and measurement validates the dimensional estimate of the gap width within (36 ± 42) nm, where the 42 nm standard uncertainty is governed by the present state of flow theory. The piston gage model is buttressed by three comparison tests against a laser barometer, which support a view that PCA2062 is linear and reproducible within 0.2 μPa Pa^{-1}. Finally, an estimate of uncertainty in the effective area of a dimensioned artifact is provided: as expected, the diameter measurement is the main culprit, but there are open questions regarding the flow model that preclude an accurate evaluation of the distortion coefficient. For the 530 kPa operating range of PCA2062, distortion is not a significant problem, but the effect would be dominant in assemblies operating at 1 MPa and above.

Keywords: piston gage, diameter metrology, mechanical pressure scale, laser barometry

1. Introduction and motivation

An experimental effort is underway to measure the refractivity of helium gas at the level of $10^{-6} \cdot (n-1)$. The motivation is that a precision measurement of helium refractivity at known temperature allows a realization of the pascal, in what is sometimes called the optical pressure scale [1]. One attraction [2] of the optical pressure scale is that it neither relies on artifacts nor restricted materials. Indeed, one stimulant to perfecting the optical realization is that it has the potential to settle the twenty-five-year-old unresolved disagreements in mechanical pressure scales—unresolved disagreements which have been at the level of $5 \times 10^{-6} \cdot p$ for piston gages [3], and $15 \times 10^{-6} \cdot p$ for mercury manometers [4]. To meaningfully conclude on past disagreements requires that one can compare

* Author to whom any correspondence should be addressed.

a new optical realization to a traditional mechanical realization at the highest levels of accuracy. This necessity for a best-effort realization of the mechanical pressure scale motivates the present work. At the National Metrology Institute (NMI) level, the outlook [1, 2, 5] is that the optical pressure scale will supersede the mechanical scale in terms of accuracy, reliability, and universality.

Toward this best effort realization of the mechanical pressure scale, three sets of piston–cylinder assemblies (PCAs) have been dimensioned, and their effective areas established as traceable to the SI meter. These state-of-the-art PCAs comprise a 50 mm diameter fixed piston with a floating and rotating cylinder. The three sets were manufactured in 2014 and coarse dimensioned in 2015. The set PCA2062 was fully dimensionally characterized in 2017. In 2020, all three sets (PCA2062, PCA2065, and PCA2066) were fully dimensionally characterized [6]. The set PCA2062 is the exemplar with the best form, and its area and performance are the main focus of this work; PCA2066 plays a role toward the end of the article. While the preceding remarks have framed this piston gage development as tandem to the optical realization, it would be remiss not to highlight the present article alone is momentous. It marks the first time that a highly accurate mechanical pressure scale has been established based on NIST dimensions. The achievement reifies a generation of dedicated effort in dimensional metrology, with a steadfast and methodical drive toward improved capability.

Next follows some details on how the dimensional datasets were converted to an effective area, which rely heavily on two references by Sabuga and coworkers [7, 8]. The procedure begins by fusing together three separate dimensional inputs (diameter, straightness, and roundness) to form a birdcage model of the artifact. Then, the pressure-induced distortion is added to the birdcage; the distortion is calculated using finite element methods, and uses one parameterized input, which is the pressure distributed down the gap between the piston and cylinder. This distributed pressure is calculated using the theory of rarefied gas dynamics. Finally, the cross-sectional area of the distorted birdcage is calculated. To explain the calculation, section 2 will logically work backwards: starting from the output (pressure equals force divided by area), and unwinding step-by-step to the input (dimensions). A block diagram of the calculation procedure is shown in figure 1(a), and the explanation will move from bottom to top. After the calculation, a lengthy discussion follows in section 3, which describes the uncertainty of a generated pressure, together with some customary diagnostics. Finally, the article concludes with section 4, which features some additional tests on piston gage performance via comparison to a highly precise laser barometer.

2. Calculation procedure

The mechanical pressure generated by the piston gage is given by

$$p_{\mathrm{mpg}} = \frac{mg}{A_0\left[1+(t_{90}-20)\,2\alpha_{\mathrm{WC}}\right](1+b\Delta p)} + p_{\mathrm{vac}}, \qquad (1)$$

where m is a mass load and g is local gravity. The effective area $A_{\mathrm{eff}} = A_0(1+b\Delta p)$ is described in more detail below, and is estimated chiefly by dimensional measurements made at $t_{90} = 20\,^{\circ}\mathrm{C}$; when the piston gage operates away from this reference temperature, its diameter (effective area) should be scaled for the thermal expansion α_{WC}. (The notation t_{90} refers to temperature measurement on the international temperature scale of 1990.) As the pressure inside the cylinder increases, the piston and cylinder deform, thus changing the diameter (effective area); the deformation parameter b accounts for pressure-induced distortion. Finally, equation (1) should balance for pressure acting outside the cylinder; in the present case, operation is in 'absolute mode' and the pressure outside the cylinder is pumped to $p_{\mathrm{vac}} < 0.3$ Pa, and measured with a capacitance diaphragm gage.

The effective area A_{eff} of the PCA should consider forces caused by flow and friction in the gap—the space between the piston and cylinder, which is approximately 580 nm. Historically, these forces were estimated by the theory of Dadson [9], which assumed viscous flow. The more recent theory of Sharipov [7, 10] is based on rarefied gas dynamics, which computes a flow coefficient determined by the level of rarefaction for all pressures and dimensions distributed down the gap. For a pressure differential across the gap $p_1 - p_2$ (in this case $p_2 = p_{\mathrm{vac}}$), Sabuga *et al* [7] write the area $A_0 = A_1 - A_2 - A_3$ as having three components [11]

$$\begin{aligned} A_1 &= \frac{\pi\,\mathcal{G}_{\mathrm{c1}}^2 p_1 - \pi\,\mathcal{G}_{\mathrm{c2}}^2 p_2}{p_1 - p_2} \\ A_2 &= \frac{\pi \int_0^{l_{\mathrm{c}}} h_z \mathcal{G}_{\mathrm{c}} \dfrac{\mathrm{d}p_z}{\mathrm{d}z}\mathrm{d}z}{p_1 - p_2} \\ A_3 &= \frac{2\pi \int_0^{l_{\mathrm{c}}} p_z \mathcal{G}_{\mathrm{c}} \dfrac{\mathrm{d}\mathcal{G}_{\mathrm{c}}}{\mathrm{d}z}\mathrm{d}z}{p_1 - p_2}. \end{aligned} \qquad (2)$$

The effective area A_{eff} is found by calculating A_0 for several different p_1, and extrapolating $(p_1 - p_2) \to 0$; the distortion coefficient b is deduced from the slope of the extrapolation. In A_0, the first component A_1 is the area upon which the mass–force acts, and depends on the radius (generatrix) at the top $\mathcal{G}_{\mathrm{c1}}$ and bottom $\mathcal{G}_{\mathrm{c2}}$ of the cylinder. The generatrix of a cylinder, described below, is obtained as the line that minimizes deviations between three sets of dimensional measurements: straightness, roundness, and point-to-point diameter. The other two components in equation (2) are A_2 and A_3, and arise from the drag forces due to gas flow in the gap and surface curvature; both of these components require knowledge of the pressure distribution p_z along the gap, and drive the gap dimensions to be updated for pressure-induced distortion. The width of the gap $h_z = \mathcal{G}_{\mathrm{c}} - \mathcal{G}_{\mathrm{p}}$ is the difference between the generatrices of the cylinder and piston. The height of the cylinder $l_{\mathrm{c}} = 40$ mm includes a 2 mm extrapolation of diameter measurements at both ends of the cylinder. The coordinate system is shown in figure 2(a): z is along the cylinder axis and x is radial; the variables $\mathcal{G}_{\mathrm{c,p}}$, h_z, and p_z are all functions of z.

The calculation is iterative [12]: first, there is a calculation of the pressure distribution from p_1 down to p_2 along the gap

$$p_z = p_1 + (p_2 - p_1)\frac{\displaystyle\int_0^z \left[h_z^2 G_\mathrm{P}\right]^{-1} \mathrm{d}z}{\displaystyle\int_0^{l_c} \left[h_z^2 G_\mathrm{P}\right]^{-1} \mathrm{d}z}, \tag{3}$$

which requires the Poiseuille coefficient [10, 13]

$$G_\mathrm{P} = a_{00} + \begin{cases} \frac{1}{2\sqrt{\pi}} \ln \frac{\mathcal{G}_c}{h} + \frac{\pi}{2} & \text{for } \delta \leqslant 5 \times 10^{-4} \\ \sum_i a_i \log(\delta)^i & \text{for } \delta > 5 \times 10^{-4}, \end{cases} \tag{4}$$

the interpolation of which is based on evaluation of the rarefaction parameter [10, 13]

$$\delta_z = \frac{p_z h_z}{\eta v_\mathrm{mp}}, \tag{5}$$

where η is the gas viscosity, and $v_\mathrm{mp} = (2RT/M)^{1/2}$ is the most probable speed and depends on the molar gas constant R, temperature T, and molar mass M. For G_P at $\delta > 5 \times 10^{-4}$, a 12th-order polynomial is fitted to the solution [10] of the one-dimensional, infinite plate, planar Poiseuille flow, with coefficients a_i

$$\begin{aligned} &a_0 = 1.547\,801 && a_1 = -1.661\,399 \times 10^{-2} && a_2 = 6.736\,396 \times 10^{-1} \\ &a_3 = 2.475\,631 \times 10^{-1} && a_4 = 1.034\,375 \times 10^{-1} && a_5 = 1.105\,164 \times 10^{-1} \\ &a_6 = 8.492\,110 \times 10^{-2} && a_7 = 2.283\,521 \times 10^{-2} && a_8 = -5.879\,727 \times 10^{-3} \\ &a_9 = -5.427\,568 \times 10^{-3} && a_{10} = -1.438\,483 \times 10^{-3} && a_{11} = -1.742\,273 \times 10^{-4} \\ &a_{12} = -8.217\,794 \times 10^{-6}. \end{aligned}$$

A numerical algorithm to calculate G_P is given in [10]. The equation (4) is plotted in figure 1(c), together with output from the algorithm of [10]. The equation (4) is modified from [10] as follows: the low rarefraction limit of equation (4) is clipped [7] as $\delta < 5 \times 10^{-4}$ to approximate the annular flow [14] in the limit $\frac{\mathcal{G}_\mathrm{p}}{\mathcal{G}_\mathrm{c}} \to 1$. This patch addresses the problem with the infinite plate solution, in which G_P becomes infinite as $\delta \to 0$. The clipping threshold is specific to each PCA geometry [7] by the quotient $\frac{\mathcal{G}_\mathrm{c}}{h_z}$. For PCA2062, even at helium pressures as low as $p_1 = 10$ kPa (and $p_2 = 0$), the annular flow approximation applies to less than 2 % of the gap region, and its influence on A_0 is negligible. The function equation (4) allows a tangential momentum accommodation coefficient of 0.9, by setting the offset factor $a_{00} = 0.25$. Lack of knowledge about the accommodation coefficient is a main contributor to uncertainty in the theory of rarefied gas dynamics; the four perturbations to G_P, plotted in the inset of figure 1(c), are relevant to the uncertainty analysis, discussed in section 3.

In the calculation of p_z, the terms p_z and δ_z are interdependent, and therefore iteration is required for convergence. (To startup, δ_z is initialized with a linear distribution of pressure down the gap.) The procedure should also be iterated for h_z, because the width of the gap changes, caused by pressure-induced distortion of the piston and cylinder. The pressure-induced distortion is computed using finite element analysis (FEA), which is parameterized for the pressure load p_z applied to the gap, obtained by calculation of equation (3). This all works with a master script, which handles several things: (i) it calculates p_z based on the most recent estimate of G_P and h_z; (ii) it dynamically updates two FEA scripts (one piston script and one cylinder) with p_z and runs the FEA program; (iii) it extracts/imports Δx along the PCA engagement region from the FEA displacement results; (iv) it updates $\mathcal{G}_\mathrm{p}$ and $\mathcal{G}_\mathrm{c}$ for the respective Δx, recomputing p_z and G_P; and (v) it iterates. An overview block diagram of the calculation procedure is shown in figure 1(a). The computed area converges within $10^{-8} \cdot A_0$ after two iterations [see figure 3(a)], and the main advantage of this 'closed-loop' implementation is that numerical investigation of model sensitivity to input errors can be performed with versatility. Another closed-loop benefit is demonstrated in figure 3(c): the effective area and distortion coefficient can be calculated throughout the cylinder's fall down the piston—something that is impractical to do with an open-loop implementation, which hand-transcribes settings from one program to another. The FEA is shown in figure 2(a), which is actually two separate simulations of a piston and cylinder, which have been clipped to the same Δx colorscale and combined (the width of the gap is arbitrarily exaggerated in x). The FEA model is axisymmetric about $x = 0$, and the boundary conditions are also annotated in figure 2(a): ① the pressure p_1 applied to the partial inner surface of the cylinder, ② the pressure p_1 applied to the inner, top, partial outer, and partial bottom surface of the piston, ③ the distributed (gap) pressure p_z applied to engaged segments of the piston and cylinder as a function of z, ④ the piston constrained in z (by a clamped o-ring), ⑤ the lip of the cylinder constrained in z (by the mass load). The distorted profiles of the piston outer diameter and cylinder inner diameter, along the region of engagement, are extracted from the FEA and added to the generatrix (dimensional measurements) in figure 2(b), with $p_1 = 500$ kPa. Figure 2(b) is also annotated with the locations of the pressure 'regions' p_1, p_z, and p_2.

The dimensional inputs to equation (2) are the generatrices of the piston and cylinder. Dimensional characterization provided high density data traces of roundness and straightness, and low density data on the point-to-point

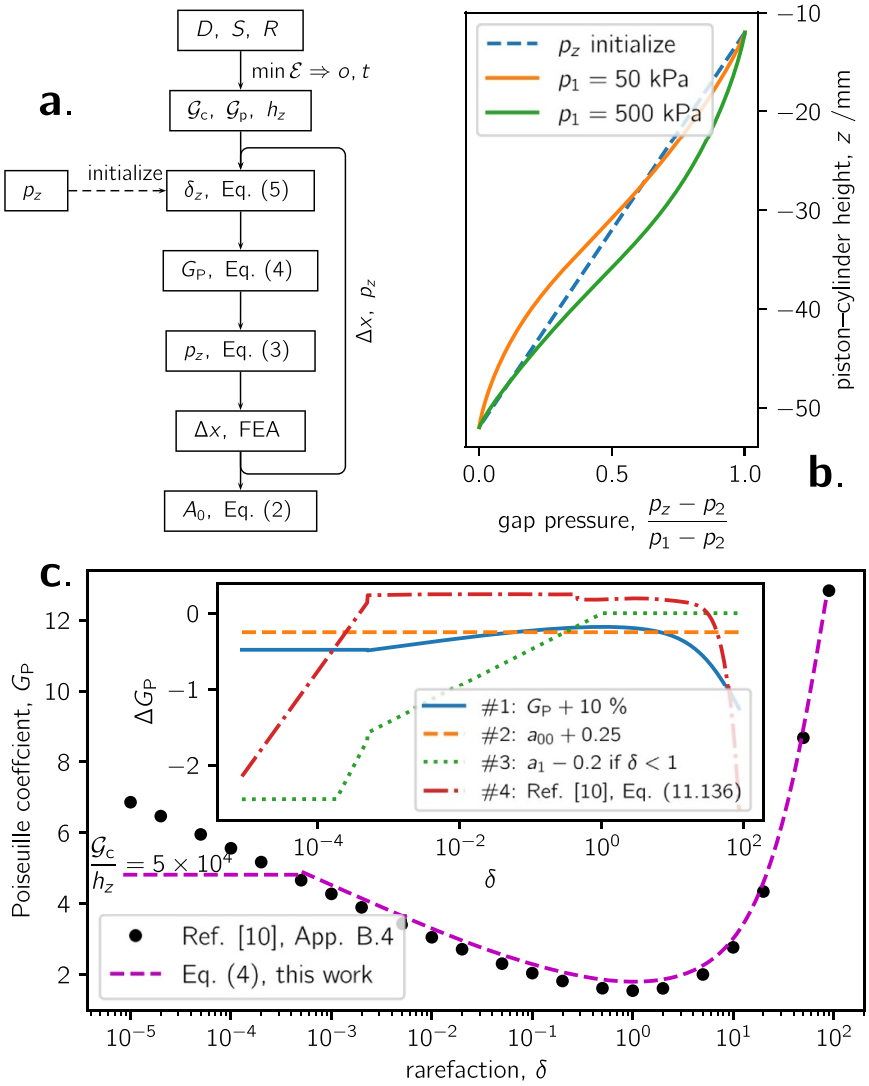

Figure 1. (a) A block diagram of the procedure to calculate A_0. (b) Pressure distribution down the gap p_z for two cases in helium, $p_1 = 50$ kPa and $p_1 = 500$ kPa, and with $p_2 = 0$. (c) The Poiseuille flow coefficient from Sharipov [10] and modified to the physical situation of the present work. The inset figure shows the difference between equation (4) and four error cases covering $u(G_P)$.

diameter. The best estimate of the artifact geometry is obtained by fusing together (synchronizing [8]) the intersecting points in the three sets of measurements. Sabuga and Priruenrom [8] found the generatrix and directrix

$$\begin{aligned} \mathcal{G}(z) &= S_\theta(z) + o + t \cdot z \\ \mathcal{D}(\theta) &= R_z(\theta) + q + w\cos\theta + v\sin\theta \end{aligned} \tag{6}$$

by adjusting the measured straightness $S_\theta(z)$ and roundness $R_z(\theta)$ by the model parameters o, t, q, w, v. Straightness $S_\theta(z)$ is a function of the height z, and is indexed for each trace made in azimuth θ; the parameters offset o and taper t are vectors of dimension equal to the number of traces in θ (which is eight for both the piston and cylinder). Roundness $R_z(\theta)$ is a function of θ, and is indexed for each trace made in z; the parameters q, w, and v are vectors of dimension equal to the number of traces in z (which is eight for the piston and five for the cylinder). The model parameters are deduced via least-squares minimization of the objective function

$$\mathcal{E}^2 = \min_{o,t,q,w,v} \sum_{i=1}^{5} \left(\frac{\sum e_i^2}{N_i} \right), \tag{7}$$

which has

$$\begin{aligned} e_1 &= \mathcal{G} - \mathcal{D} \\ e_2 &= \frac{D - (\mathcal{G} + \mathcal{G}')}{2} \\ e_3 &= \frac{D - (\mathcal{D} + \mathcal{D}')}{2} \\ e_4 &= \frac{D_{\text{ref}}}{2} - \mathcal{G}_{\text{ref}} \\ e_5 &= \frac{D_{\text{ref}}}{2} - \mathcal{D}_{\text{ref}}, \end{aligned} \tag{8}$$

and D are the measured point-to-point diameters. (The term $\mathcal{E}$ is the root-mean-square error of the optimization, and is a

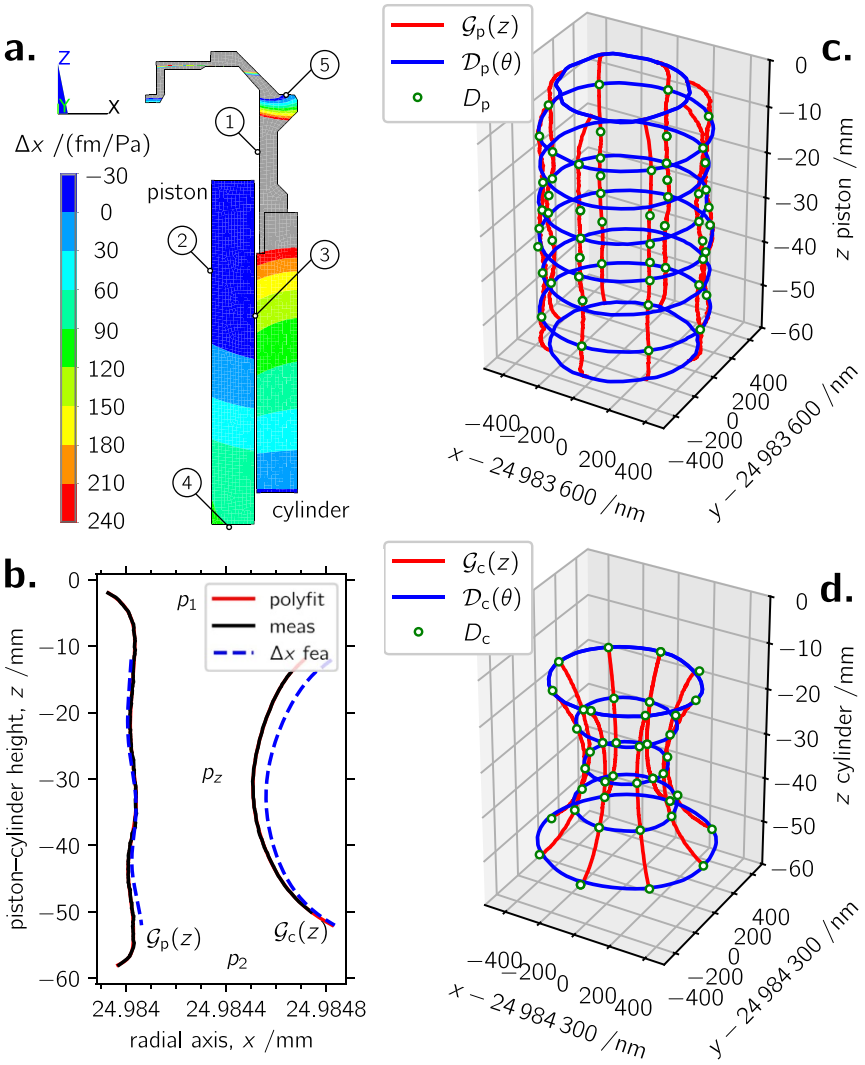

Figure 2. (a) The finite element model of pressure-induced distortion in the piston and cylinder. (b) Least-squares-adjusted generatrices of the piston and cylinder, with overlay of pressure-induced distortion at $p_1 = 500$ kPa and $p_2 = 0$. (c) and (d) A 'birdcage' model of the piston and cylinder, constructed by fusing three sets of dimensional data: straightness, roundness, and point-to-point diameter.

metric of statistical uncertainty. The integer N_i is the sample size of each residual error matrix e_i.) The flow calculation of Sabuga *et al* [7] uses the generatrix $\mathcal{G}$ of the piston and cylinder to calculate the cross-sectional area that best describes a three-dimensional artifact. The residual matrices e_4 and e_5 in equation (8) are set up as reference points to define the coordinate system in which the dimensional adjustment is performed. This means they are set up as sparse matrices of four diameters; two at different z heights, and two at different θ azimuthal angles. The choice of height and angle is arbitrary. The notations $\mathcal{G}'$ and $\mathcal{D}'$ refer to the generatrix and directrix, respectively, at the opposite azimuthal orientation.

The least-squares adjusted datasets are shown in figures 2(c) and (d); these plots are sometimes called the 'birdcage' [15, 16]. The plot of the piston in figure 2(c) has been scaled in the radial axis by subtracting 49.9672 mm from the diameter; the plot of the cylinder in figure 2(d) has had 49.9686 mm subtracted from the diameter. Once the vectors o and t have been found by the least-squares adjustment of the intersecting points, each straightness trace can be converted to its respective $\mathcal{G}$. The result is a set of eight $\mathcal{G}$, which are a function of z, and are indexed for each straightness trace in θ. For calculation of A_0, the eight $\mathcal{G}$ are averaged over θ.

Finally, this dimensional characterization of $\mathcal{G}$ is used in the area calculation of equation (2), to produce a determination of $A_0 = A_1 - A_2 - A_3$ as a function of pressure. The A_0 result is plotted in figure 3(b); the relative contributions of A_2 and A_3 are shown in the inset of figure 3(b). From this, the effective area of PCA2062 has been determined as

$$A_{\text{eff}}^{2062} = 1961.0292\,(37)\left[1 + 5.12\,(73) \times 10^{-12}\,\frac{\Delta p}{\text{Pa}}\right]\ \text{mm}^2$$

in helium at 20 °C and absolute mode, and is valid for the dimensional characterization of 2020. The distortion coefficient b is best described by a linear term. The estimation of b from the slope of the line in figure 3(b) is for a monolithic assembly. The final estimate given above is 2.6 % smaller than

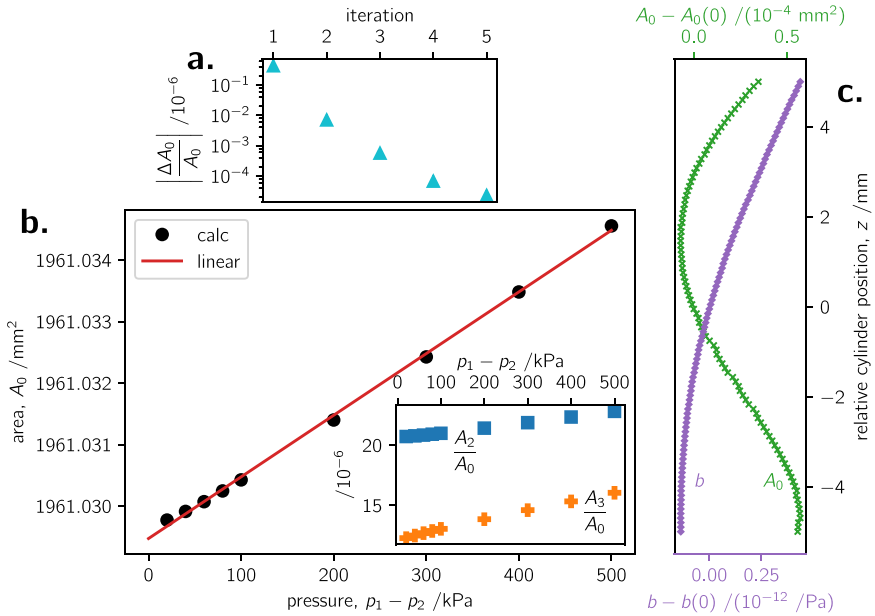

Figure 3. (a) Convergence of the p_z and FEA iteration loop. (b) The calculated area as a function of pressure for the piston–cylinder assembly PCA2062 in 'absolute mode' with $p_2 = 0$. Inset: relative contributions of A_2 and A_3 to A_0. (c) The change in A_0 and b, relative to values at $z = 0$, as the cylinder falls down the piston.

the slope of the line in figure 3(b); this reduction in distortion is based on a finite element simulation of a 0.1 mm epoxy joint between the titanium (cap) and tungsten carbide that forms the hollow cylinder assembly. What follows next is the uncertainty budget for this determination.

3. Uncertainty evaluation

The uncertainty budget for the pressure generated by a piston gage is given in table 1. Most entries concern the proportional term, but there are two entries which are best split into an offset term. With this splitting of terms, the combined uncertainty is slightly overestimated in parts of the pressure range. But the general message is that uncertainty is dominated by the proportional term throughout most of the working range. It is only below 50 kPa that the offset term becomes significant (which is the lower tenth of the working range).

The budget in table 1 evaluates each input parameter to equation (1), and the entries in the table are discussed below. Some of these assessments may be considered controversial, due to their relative largeness compared to antecedent estimates of piston gage uncertainty; here, the intention is to be conservative rather than controversial. Throughout this article, the notation $u(x)$ is used to denote the standard uncertainty of the quantity x. Unless otherwise stated, all uncertainties in this work are one standard uncertainty, corresponding to a confidence level of approximately 68 %.

3.1. The main contributor, $u(A_0)$

3.1.1. Dimensional uncertainty. Diameter measurement was a massive effort, and required the improvement of an old instrument (sphere diameter in a Fizeau-type interferometer) [17], the establishment of a new instrument (cylinder and sphere diameter in a laser micrometer) [18], and two forty-year-old coordinate-measuring machines (CMMs) in pristine condition. The breadth and scope of the development is described by Stoup *et al* [6], and here only a brief synopsis is provided. The outer diameter of the piston was measured with an ultrahigh accuracy laser micrometer. The inner diameter of the cylinder was measured with the CMM in comparison mode: the CMM effectively operated as a null-comparator, comparing the (unknown) diameter of the cylinder relative to the (known) diameter of the piston. The probe of

Table 1. Relative standard uncertainty in mechanical pressure generated by a dimensioned piston gage has been split into an offset and proportional term.

Component	$u(p_{\mathrm{mpg}}) \times 10^6$	
A_0		
dimensional		1.7
D, 13 nm		
$\mathcal{E}$, 19.8 nm		
extrapolation, 10 nm		
α_{WC}, 4.6 nm		
compression, 3 nm		
instability, 17.8 nm		
flow		0.7
RGD, 2.9×10^{-4} mm^2		
$\mathcal{G}$, 13×10^{-4} mm^2		
h_z, 0.1×10^{-4} mm^2		
b		0.4
m	54 mPa +	0.1
g		0.2
p_{vac}	2.5 mPa	
combined ($k = 1$)	$\left[(54\ \mathrm{mPa})^2 + (1.9\ \mu\mathrm{Pa\ Pa}^{-1})^2\right]^{1/2}$	

the CMM was mastered with precision spheres, whose diameters were independently determined with the Fizeau-type interferometer. These master spheres also provided a crosscheck between the Fizeau-type interferometer and the laser micrometer. Additional reference artifacts and crosschecks were strategically employed in the characterization to achieve state-of-the-art performance in a CMM-as-comparator: reference [6] has the details. One strength of this diameter measurement is redundancy, with different artifacts being cross-validated across multiple measuring machines, and each machine having its own unique and understood systematic errors. The uncertainty [6] for the piston diameter (outer) was 12 nm, and the uncertainty for the cylinder diameter (inner) was 14 nm. The entry D in table 1 treats the two diameters as fully correlated, and the net uncertainty in the effective diameter of the assembly is $[u(D_\mathrm{p}) + u(D_\mathrm{c})]/2$.

In addition to the measurement uncertainty in diameter, there is uncertainty in how well the three-dimensional datasets can be fused together [6]. The least-squares adjustment described by equations (6) and (7) builds a generatrix and directrix to form a model birdcage—a wireframe whose coordinates depend on the intersecting points of the diameter, straightness, and roundness. Residual deviation persists between the three datasets, because each measuring machine has its own error, and there are likely small changes in orientation/indexing as the artifacts are moved between machines and measured. This residual deviation means that there is statistical uncertainty in the generatrix $\mathcal{G}$. The estimate of this statistical uncertainty is the entry $\mathcal{E}$ in table 1. The term $\mathcal{E}$, defined in equation (8), is the root-mean-square error of the objective function after minimization, and reflects the net deviation between the three error matrices, $\mathcal{G}-\mathcal{D}$, $D/2-\mathcal{G}$, and $D/2-\mathcal{D}$. The result for the piston $\mathcal{E}_\mathrm{p} = 4.8$ nm, and for the cylinder $\mathcal{E}_\mathrm{c} = 8.5$ nm; these computed results are in terms of the radius. Attempts were made [6] to estimate residual strain in the birdcage, and assess the flexibility available to $\mathcal{G}$ due to lack of coverage in the D,S,R-dataset. This investigation was done by Monte Carlo simulation. The idea was to deliberately remove dimensional data from the birdcage, and simulate the resulting effect on $\mathcal{G}$. The conclusion from simulation was that $\mathcal{E}$ adequately covers all expected variation in $\mathcal{G}$, for birdcage sampling as dense as figure 2(c) or (d). The entry $\mathcal{E} = (\mathcal{E}_\mathrm{p}^2 + \mathcal{E}_\mathrm{c}^2)^{1/2}$ in table 1 treats the imperfect form of the piston and cylinder as uncorrelated in their contribution to uncertainty in the effective diameter of the assembly. Finally, the component $\mathcal{E}$ only covers the uncertainty in fusing together three-dimensional datasets; a related component—the effect of imperfect cylindricity on flow—is a separate entry, discussed below.

Mechanical probing can only approach the actual 'edge' defining the end of the piston and cylinder, because of the finite probe size and instability in fixturing. Therefore, extrapolation is used to estimate the cylinder diameter. As seen in figure 2(b), the measured cylinder radius is increasing by approximately 25 µm m^{-1} at the extremity; therefore, $\mathcal{G}_\mathrm{c}$ should be extrapolated across 2 mm to determine the diameter at the point of engagement. Because the cylinder of PCA2062 has a uniquely smooth and predictable curvature, one can have confidence in this extrapolation within 10 %. This uncertainty component is labeled 'extrapolation' in table 1. This extrapolation of the diameter measurements to the cylinder end increases the effective area by $3.5 \times 10^{-7} \cdot A_0$.

Deviations from the 20 °C reference temperature at which the piston and cylinder were dimensioned should be compensated for thermal expansion of the artifacts. For typical use, the piston gage PCA2062 operates in a lab stabilized to (20 ± 0.1) °C, and the small corrections for thermal expansion require moderately accurate thermometry of the PCA. The temperature of the PCA was measured using onboard resistance thermometers; these resistance thermometers were calibrated near 20 °C by direct comparison to a calibrated thermistor, all placed in an isothermal block. The uncertainty in this calibration procedure is within a few millikelvin, and despite operating in a laboratory with very small thermal fluctuations and gradients, a 20 mK uncertainty is assigned to the temperature of the PCA. The relatively large assessment is because the resistance thermometer is inside the post of the piston gage, and does not directly measure the temperature of the PCA; the 20 mK covers gradients that potentially develop between the thermometers and PCA. For the thermal expansion coefficient of tungsten carbide, the nominal value $\alpha_\mathrm{WC} = 4.6 \times 10^{-6}$ K^{-1} is used. For the 20 mK uncertainty in the PCA temperature, the 50 mm diameters can therefore be confidently compensated for temperature within 4.6 nm. This component is labeled α_WC in table 1. Because the nominal value α_WC is used, this temperature dependent diameter uncertainty is only valid for operation near 20 °C.

A component 'compression' is added to the budget, which accounts for uncertainty in the piston diameter, because it is clamped between two o-rings. Although the effect is small—the change in diameter $\Delta D \approx \frac{4\mu F}{\pi D E}$, given by Poisson's coefficient μ and Young's modulus E—it is difficult to have confidence in the compression force F of the clamped o-ring, and possible 'barreling' caused by friction. Manufacturer handbooks give rules-of-thumb, based on o-ring durometer, diameter, and compression, suggesting a clamping force of approximately 2.6 N mm^{-1} of the lineal o-ring. The rule-of-thumb is assumed reliable within a factor of 2, which yields the 3 nm uncertainty in the diameter caused by o-ring compression force. [Another 'compression' that should be considered is compressibility of the PCA, because the artifacts are dimensioned at atmospheric pressure, but operate in vacuum (absolute mode). Compressibility is accounted for in the FEA of figure 2(a), and only changes area by $2 \times 10^{-7} \cdot A_0$. Its uncertainty contribution is effectively absorbed into $u(\mathcal{G})$, discussed below.]

The last dimensional component in table 1 is instability of the artifacts. The assembly PCA2062 was initially dimensioned in 2017. Its calculated area from the 2017 dimensioning was 0.2 µPa Pa^{-1} smaller than the present report. The mean piston diameter was 18.8 nm smaller; the mean cylinder diameter was 16.8 nm larger. At this level, and with only a two-sample history, it is not clear whether the gage is unstable, or if the reproducibility in the measurement procedure is being validated, or if wear is a possible explanation. (Based on almost identical straightness and roundness

Table 2. Comparison of the experimental fall rate to theory and equation (9). PCA2062 in absolute mode, $p_2 < 0.3$ Pa. The numbers in brackets express standard uncertainties. The viscosities used are from REFPROP [28], which at 293.15 K are: $\eta_{He} = 19.63$ μPa s, $\eta_{Ar} = 22.31$ μPa s, and $\eta_{N_2} = 17.57$ μPa s.

	v_{fall}/nm s^{-1}								
	Helium			Argon			Nitrogen		
p_1 /kPa	exp.	theory	% diff.	exp.	theory	% diff.	exp.	theory	% diff.
43	609(66)	652(75)	−6.6	180(19)	200(24)	−10.2	209(23)	239(28)	−12.6
93	597(64)	639(76)	−6.6	207(22)	221(24)	−6.4	245(26)	267(29)	−8.5
195	651(70)	694(79)	−6.1	273(30)	287(25)	−4.7	330(36)	352(31)	−6.3
297	726(78)	781(82)	−7.0	349(38)	367(33)	−4.9	417(45)	453(40)	−8.0
399	806(87)	887(85)	−9.1	442(48)	458(41)	−3.4	519(56)	569(50)	−8.6
501	908(98)	1009(91)	−10.0	546(59)	559(49)	−2.2	648(70)	695(61)	−6.8

traces in both dimensional datasets between 2017 and 2020, it is felt that wear is an unlikely explanation.) Nevertheless, at this early stage of the gage's control chart, a 17.8 nm uncertainty is assigned to temporal stability of the artifact's dimensions. Additional dimensional checks over the next decade may reduce this uncertainty component.

3.1.2. Flow uncertainty. No clear uncertainty budget has been developed for the rarefied gas dynamics model of Sharipov. Lacking this knowledge, first, for the present geometry, the classical Dadson theory predicts A_0 to be 2×10^{-7} smaller than Sharipov. (As Sutton and Fitzgerald [19] have highlighted, viscous flow—Dadson theory—has almost no application to modern PCAs, with 500 nm gap widths operating sub-megapascal. Nevertheless, Sutton and Fitzgerald [19] also argued that the choice of flow model only influences A_0 at fractions of a part per million. This fact was verified by Sabuga [20]. The present work agrees that A_0 is weakly dependent on the flow model.) Second, reasonable uncertainty estimates for the viscous slip coefficient have a negligible effect on G_P (and A_0, shown by Sharipov *et al* [21]). Last, an attempt was made to estimate the error bounds on G_P based on information provided by Sharipov and Seleznev [22] and Sharipov [10]. The largest uncertainty component in G_P is the tangential momentum accommodation coefficient, which describes energy transfer at the gas–surface interface [23]. The coefficient is an experimental input to the scattering kernel that underpins the theoretical calculation [13, 24] of G_P; the coefficient is unity for perfectly diffuse scattering, and zero for specular reflection. This accommodation coefficient is species- and roughness-dependent, and for polished tungsten carbide, is unknown. Surveys [24, 25] of measurements for the accommodation coefficient show much variability, and concludes [25] that a 'range of 0.80–1.02 seems to encompass almost all data available in the literature for monatomic gases irrespective of the Knudsen number and surface material.' A more recent extraction from highly accurate acoustic resonator experiments in helium and argon also showed some variability [26], and noted that the derivation of an accommodation coefficient from experimental data is non-trivial. Since no information is available for the accommodation coefficient of polished tungsten carbide, reference [25] is used as a guideline, and a value of 0.9 ± 0.1 is assumed. Sharipov *et al* [10, 13, 22] show that an error of 0.1 in the accommodation coefficient causes, to the first order, a 0.25 offset in G_P throughout the rarefaction range; a smaller accommodation coefficient increases G_P. Sharipov *et al* [10, 22] also show that the choice of kinematic model used to approximate the Boltzmann equation can cause an error of 20 % in G_P, where deviation is most prominent $\delta < 1$. Based on these arguments, $u(G_P)$ was evaluated by propagating four error cases through the A_0 calculation: (i) a 10 % increase in G_P resulted in -0.1×10^{-4} mm^2; (ii) a 0.25 increase in a_{00} resulted in $+0.5 \times 10^{-4}$ mm^2 (i.e., the effect of error in the accommodation coefficient); (iii) a 0.2 increase in a_1 when $\delta < 1$ resulted in $+1.4 \times 10^{-4}$ mm^2 (i.e., the effect of error approximating the Boltzmann equation); (iv) the three-part interpolation function, equation (11.136) in [10], for G_P resulted in $+0.4 \times 10^{-4}$ mm^2. The difference between equation (4) and each of the four G_P error cases is graphically shown in figure 1(c). Therefore, the component 'RGD' added to table 1 is a combination of half the error between rarefied gas dynamics versus Dadson theories, plus half the range of the four error cases which cover $u(G_P)$. This is a best estimate of what contribution the uncertainty in the rarefied gas dynamics model makes to $u(A_0)$, but it is based on limited information.

Despite these open questions about uncertainty in flow theory, the Sharipov model does predict the fall rate [21]

$$v_{fall} = \frac{v_{mp}^2}{2\pi \mathcal{G}_c^2 p_1} \dot{m}, \tag{9}$$

for a mass flow rate [27] $\dot{m} = -\frac{\pi(\mathcal{G}_p + \mathcal{G}_c)}{v_{mp}} G_P h_z^2 \frac{dp_z}{dz}$. The generatrices in these formulae refer to the pressure-distorted profiles. A comparison of theory with what is observed experimentally is listed in table 2, for the gas species helium, argon, and nitrogen. The estimate of uncertainty in the theoretical fall rate is between 10 % and 14 %, and comes from half the range of v_{fall} calculated for the four error cases covering $u(G_P)$, described above. The theoretical values have assumed $a_{00} = 0.25$ in the G_P function equation (4) for all gases (i.e., a tangential momentum accommodation coefficient of 0.9 for all gases interacting with polished tungsten carbide). For experiment, $u(v_{fall})$ is 10.8 %: the measurement of the cylinder position has an uncertainty of 10 % in the length scale (which was

Table 3. Comparison of rotational-decay rates between experiment and theory in equation (10). Moments of inertia I for the rotating assembly are listed, which correspond to the mass loads generating the pressures p_1 of table 2. PCA2062 in absolute mode, $p_2 < 0.3$ Pa. The numbers in brackets are standard deviations on ten repeat measurements.

	$\frac{\Gamma}{I}$ /(μs^{-1})								
	Helium			Argon			Nitrogen		
I/kg m^2	exp.	theory	% diff.	exp.	theory	% diff.	exp.	theory	% diff.
0.023	1296(168)	1217	6.4	2430(170)	2681	−9.4	2161(161)	2182	−0.9
0.171	265(16)	276	−3.9	583(11)	517	12.8	433(19)	416	4.0
0.467	156(18)	148	4.9	250(4)	238	5.3	197(4)	190	3.5
0.763	104(4)	106	−1.5	169(6)	158	7.2	133(4)	126	6.4
1.059	84(2)	83	0.0	121(8)	118	2.9	101(7)	93	7.7
1.355	70(1)	68	2.1	95(2)	93	2.1	83(5)	74	11.9

calibrated with calipers), and the reproducibility in the measurement is within 4% (one standard deviation on ten measurements). Referring to table 2, the experimental v_{fall} agrees with the theory within 8 % on average for all three gas species. For helium, it is remarkable that both experiment and theory show a reduction in v_{fall} as p_1 increases from 43 kPa to 93 kPa. These two facts give confidence in the validity of the flow model (and increase the confidence in the FEA distortion model). Two concerns are noted: (i) disagreement between experiment and theory appears systematic for all three species, suggestive of either the measured gap width being too wide or the theoretical G_{P} being too high; and (ii) a quantitative validation of the flow model requires a dedicated experiment to measure the accommodation coefficient for each species interacting with polished tungsten carbide. (Qualitative information from the literature survey of [25] suggests that the accommodation coefficient for argon would be 0.03 lower than that of helium—hence G_{P} is larger, and the theoretical v_{fall} is faster by about 7.5 % than that listed in table 2.)

Additionally, the Sharipov model—Poiseuille flow with no-slip boundaries—does not presently describe the effect of rotation. A phenomenological account is due to Schmidt *et al* [29], who modeled decay in the rate of rotation as having a period $\tau = \tau_0 \exp\left(\frac{\Gamma}{I}t\right)$, where Γ is the angular torque coefficient and I is the mass moment of inertia. Schmidt *et al* used a momentum transfer function to interpolate the torque coefficient between two limiting cases, i.e., viscous and free-molecular flow regimes. The final expression for the torque coefficient, a drag caused by gas in the annular region between the piston and rotating cylinder,

$$\Gamma_{\text{an}} = \frac{2\pi \mathcal{G}_{\text{c}}^3}{h_z} \int_0^{l_{\text{c}}} F(p_z)\,\mathrm{d}z, \tag{10}$$

includes the momentum transfer function $F \equiv \frac{\eta}{1+\beta/p_z}$, with the variable $\beta = \frac{2\sqrt{\pi}RT\eta}{M v_{\text{mp}} h_z}$ chosen for smooth interpolation between the two limiting cases of the flow. Experimental estimates of $\frac{\Gamma}{I}$ are obtained as the slope of a linear fit to the measured period of rotation $\ln(\tau)$ as a function of time. In the absolute mode of operation $\Gamma \approx \Gamma_{\text{an}}$, because the contribution of drag on the rotating surfaces in the bell jar is considered negligible (i.e., the bell jar pumped to $p_2 < 0.3$ Pa). Therefore, equation (10) can be compared to experimental measurements of rotation decay rates; this comparison is listed in table 3. Schmidt *et al* [29] used equation (10) to deduce h_z by regressing experimental data to the model; upon encountering a discrepancy between h_z inferred by the fall rate versus rotational-decay, they stated a preference for the latter inference. In the present case, close agreement between experiment and theory, for both the fall rate (table 2) and rotational-decay (table 3), tends to increase confidence that the artifact is understood; besides the fact that h_z is claimed to be known within 7.3 % (41 nm) by dimensional measurement. However, it must be pointed out that equation (10) is a makeshift combination of p_z from rarefied gas dynamics [7] combined with the interpolation of limiting cases suggested by [29]. The purpose of this paragraph was to draw attention to the need for cylinder rotation to be incorporated into the rarefied gas dynamics model of the piston gage in a rigorous way, together with a quantitative statement with regard to the magnitude of vertical force on a spinning irregular shape.

The much larger uncertainty component in the flow calculation is related to the generatrix and the imperfect geometry of the artifact. Despite the adjustments o and t to the dimensional measurements, A_0 has a variance related to variability among $\mathcal{G}$. As an example, the out-of-roundness of the piston and cylinder are about 60 nm at the point of engagement. In principle, under the assumptions of viscous flow [10] (hydrodynamic regime) and axisymmetry (or, no rotation), this imperfect form can be accounted for by performing the flow calculation for each azimuthal $\mathcal{G}$ as a continuum [30]. However, continuity is not always valid in the theory of rarefied gas dynamics [22, 23, 31], and the assumption of axisymmetry is questionable, because out-of-roundness is six to nine times larger than uncertainty in a single diameter measurement. Instead, the present view accepts that imperfect geometry introduces an uncertainty component into the calculation of A_0. This component was evaluated by iterating the calculation of A_0 for all 64 permutations of piston and cylinder generatrices (azimuthal orientations); in effect, rotating the cylinder around the piston. The standard deviation on the 64 calculations was 1.1×10^{-3} mm^2. (The range was 4.4×10^{-3} mm^2; the authoritative work of Schmidt *et al* [16] used one half of the range as standard uncertainty. The mean of the 64 permutations of A_0, based on combinations of $\mathcal{G}$, agrees with A_0 calculated by the azimuthal average, within 1 part in 10^7; the median of the

64 permutations is 2.0×10^{-8} larger than the mean.) Again, the dimensional measurements of roundness and straightness stop 2 mm short of the cylinder end, and the out-of-roundness trends at 2.6 nm mm^{-1} worse toward the end: therefore, it is projected that the effect of out-of-roundness is about 10 % larger than what the 64 permutations suggest. Also, polynomial fits to the measured $\mathcal{G}$ data are used (i.e., to extrapolate $\mathcal{G}_c$, and for numerical advantage) but this 'filtering' may remove actual surface features. The standard deviation on the residuals from the fit is less than 1.5 nm, and the range is 9.5 nm: at this dimensional level, it is not clear if the polynomial fitting removes surface features or measuring-instrument noise. Nevertheless, if the 'raw' measurement data are used for computation, the difference from that obtained for the polynomial fits is only $3 \times 10^{-9} \cdot A_0$. Therefore, the entry $\mathcal{G}$ in table 1 is predominantly because of imperfect cylindricity.

The width of the gap h_z varies as the cylinder falls down the piston. For the geometry of historic PG39, Jain *et al* [15] estimated that geometric effects would change the area by $1 \times 10^{-6} \cdot A_0$ as the piston moved 3.5 mm relative to the cylinder in z; Sharipov *et al* [21] found a difference of $0.7 \times 10^{-6} \cdot A_0$ between low and high positions (i.e., relative positions of the piston and cylinder that differed by 5.5 mm in z). In the present work, this effect was evaluated by iterating the calculation of A_0 as the location of the cylinder incrementally moves down the piston; in effect, sliding a window across the portion of $\mathcal{G}_p$ that is used in equation (2) and loaded with p_z in the FEA. The result is shown in figure 3(c); the valid 'float zone' is the cylinder position range ± 2.5 mm, where A_0 has a dependence of 4.0×10^{-5} mm^2 mm^{-1}. The result of figure 3(c) can be intuitively explained: A_0 reaches a maximum as the cylinder falls past the small bump in the piston profile (see figure 2(c) at $z \approx -33$ mm), while b steadily decreases as more of the piston outer diameter is loaded with p_1. (To be clear, the piston is becoming more distorted as the cylinder falls; therefore, the average diameter of the PCA decreases and A_{eff} decreases.) The piston gage has a position sensor which can monitor cylinder height within 0.2 mm. Thus, one can either record a generated pressure at a reference cylinder height corresponding to a specific calculation of A_{eff}, or compensate A_{eff}, depending on the indication of the cylinder height. The estimate of the h_z variation in table 1 is therefore a small effect overall, for the unique geometries of PCA2062. (Measurement corroborating this calculated h_z effect follows in section 4.)

3.1.3. Summary of $u(A_0)$. In the dimensional entries for A_0 in table 1, 'extrapolation' and 'compression' are treated as biases, and therefore add half their estimate in quadrature with the other entries. The quadrature sum of the dimensional and flow entries results in $u(A_0)$ contributing 1.7 µPa Pa^{-1} uncertainty to a generated pressure, and is thus the dominant component. Arguments can be made that the entries $\mathcal{E}$ and $\mathcal{G}$ are duplicates, which effectively sample the same source of uncertainty—imperfect cylindricity—and therefore the uncertainty is slightly overestimated. Although the origin of both entries is probably the same, they are interpreted as separate and unrelated. The entry $\mathcal{E}$ is viewed as describing the uncertainty in how well a static set of 3D dimensional measurements can be fused together and represented by a cross-sectional profile. The entry $\mathcal{G}$ is viewed as describing the uncertainty in forces arising from non-continuous flow, as a non-axisymmetric cylinder rotates about a non-axisymmetric piston. In section 4, indirect tests on the effect of rotation on the generated pressure suggest that the entry $\mathcal{G}$ is overestimated by a factor of five for PCA2062 (or a factor of two for more typical PCAs); the entry $\mathcal{G}$ is therefore precautionary, and its removal awaits a theoretical estimate of the effect of rotation on flow.

3.2. Minor contributors

Knowledge of the distortion coefficient b is limited by uncertainty in elastic properties, the accuracy of the pressure distribution in the gap, and the fidelity of the finite element model to the experiment. Salama *et al* [32] demonstrated that the elastic properties of tungsten carbide might be measured within 0.1 % via resonant ultrasound spectroscopy; the PCA analyzed here is made from the same sintering of tungsten carbide as measured by Salama *et al*, but [32] also showed that variations exist between batches of up to 4 %. Changing the material properties by 4 % in the model resulted in a change of 1.6% to b. From the dimensional discussion above, the gap width h_z is confidently known within 41 nm. Changing the h_z input to the model by 41 nm resulted in a change of 1.6 % to b. The aforementioned 64 permutations for the piston and cylinder over all azimuthal orientations showed a standard deviation in b of 9.2 % (this uncertainty is partially accounted for by $u(\mathcal{G})$ above). Also, figure 3(c) shows that b can vary by as much as 6.4 % as the cylinder falls down the piston; the effect is ten times smaller if a correction is applied for cylinder height. Finally, the pressure distribution in the gap depends on knowledge of G_P, and the quadrature sum of the four error cases covering $u(G_P)$ was an uncertainty of 10.2 % in b. Validation of the finite element model is less straightforward. Neither increasing the density of the mesh, nor sample spacing on p_z, influenced b by more than 0.01 %; both the element edge size and step size in z were 0.1 mm. However, it is less certain that the boundary conditions accurately reflect the real world. The piston is modeled as free to deform, and thus does not properly account for the friction of the clamped o-ring. The effect of this oversight should be small, because the piston distorts five times less than the cylinder. Furthermore, the PCA plumbing has a 'controlled clearance port', which allows the pressure applied to the internal surfaces of the piston to be independent of p_1: this feature offered an indirect validation of the FEA estimate of piston distortion, via a change in the fall rate and h_z in equation (9). If the inside surface of the piston remains at atmospheric pressure, the FEA predicts an increase in v_{fall} of 11 % at $p_1 = 500$ kPa, whereas experiment showed a 13 % increase in v_{fall}. This agreement suggests that o-ring friction has a small effect on piston distortion, and piston distortion makes the smaller contribution to b. For the cylinder, it is modeled as a monolithic joint between the tungsten carbide cylinder and titanium cap; in reality, the two parts are epoxied together. If a 0.1 mm layer of epoxy ($E = 1$ GPa, $\mu = 0.4$) is

introduced between the cylinder and cap, b decreases by 5.2 %. (The value stated above $b = 5.12(73) \times 10^{-12} \cdot \frac{p}{\mathrm{Pa}}$ is the mean of the monolithic and epoxy models.) By adding in quadrature all the aforementioned variations in b, one can only claim confidence that the finite element model can predict b within 13.9 %, with the main uncertainty due to $u(p_z)$—i.e., because G_P is not very well known. The statement in table 1 that b contributes no more than 0.4 μPa Pa^{-1} to a generated pressure is valid for the piston gage operating within its specified range $p_1 - p_2 < 530$ kPa.

The mass load is predominantly made of a stack of nine 10.2 kg stainless steel masses, one 6.4 kg stainless steel mass, a titanium mass bell/pan, together with the cylinder of the PCA (a tungsten carbide cylinder with a titanium cup); the non-stainless steel part of the mass load, which contributes to every generated pressure, amounts to 2.1 kg. The stainless steel masses were made of 316 alloy with magnetic susceptibility less than 0.01. The masses were calibrated in air within 35 ng g^{-1} standard uncertainty. However, because the piston gage operates in absolute mode, the buoyancy correction to convert the (conventional) mass calibration values to vacuum (true) mass also comes into play. The density of the masses was obtained by hydrostatic weighing of a material token in fluorocarbon [33], from which (7981 ± 10) kg m^{-3} was deduced. The resulting uncertainty in the stainless-steel component of the mass load is 0.1 μg g^{-1}. A lack of accurate knowledge in the density of titanium and tungsten carbide is best handled by a 8.1 mg offset term (an uncertainty in density of 4 %). Additional offset terms [34] arise from two unstable masses: (19 ± 7) mg vacuum grease on one screw thread to prevent binding, and an elastomer o-ring subject to (0.2 ± 0.04) mg desorption of water [35]. (Šetina *et al* [35] report a mass gain of 2 mg by water absorption into a 2.6 g o-ring; the pressure balance o-ring is 0.22 g, and of the same elastomer.) The quadrature sum of these three mass offset terms equates to the 54 mPa in table 1.

Lastly, the two remaining components in table 1 are discussed. Local gravity was measured with a free-fall gravimeter, and was updated for seasonal changes. The estimate of $u(g)$ also accounts for imperfect leveling of the PCA. The vacuum gage has an indication uncertainty of 0.5 %, and the bell jar pressure, which is turbopumped, was always less than 0.5 Pa.

4. Pretensions of laser barometry

This closing section describes some tests between a laser barometer and a piston gage. These tests say some interesting things about precision and consistency of the A_0 and b calculation described above. (For more details on laser barometry, see section IV of [36] and references therein.)

The laser barometer was plumbed directly to the piston gage system. The setup for the laser barometer is similar to [37], in which a monolithic homogeneous Fabry–Perot cavity is suspended from cables and probed with a 633 nm laser. The laser mode between the mirrors of the cavity has been enclosed within a copper block, and the temperature of this copper block was measured with a capsule-type standard platinum resistance thermometer. (The copper block does not touch the glass cavity.) This key feature achieves the following system characteristics: for a 112 kPa charge of argon, the settling time required for the temperature gradient between the thermometer and cavity mode to reach 0.1 mK is within 1500 s, with a time constant of 360 s. The performance has been verified by simulation and indirect measurement. These extra details about thermal characteristics are not misplaced. The tests below demonstrate precision and reproducibility in the optical pressure at the level of ±0.1 μPa Pa^{-1} for pressures up to 500 kPa. A ±0.1 μPa Pa^{-1} precision in optical pressures is equivalent to claiming that a capsule-type standard platinum resistance thermometer, distant from the laser beam, inferred an average gas temperature along the cavity mode within ±30 μK. The claim is extreme, but it is supported.

Next follows a description of three tests, in which the reproducibility and precision of the optical pressure scale are used to validate three aspects of the piston gage model and performance. Below, the notation $p_\mathrm{ops} = \frac{2}{3A_\mathrm{R}}(n-1)RT + \cdots$ is used to refer to the optical pressure scale, realized by measurement of argon refractivity $n - 1$ at a known temperature T. (The molar gas constant R is a fixed value; the molar refractivity A_R is a reference property of argon gas.) However, the purpose of this closing section is cross-validation via relative differences and ratios; these tests say nothing about the accuracy of either A_eff^{2062} or the properties of argon.

4.1. Effect of cylinder position

A first test used the laser barometer to monitor the small changes in the generated pressure as the cylinder fell down the piston. From figure 3(c), the piston gage model predicts that the area and distortion coefficient will change. Therefore, the first test compared a generated (calculated) pressure p_mpg to an optical (measured) one p_ops as a function of the cylinder position.

The result is plotted in figure 4(a) for operation at $p =$ 469 kPa, where a fractional change in pressure is shown as a function of the cylinder position (fall). For the x-axis, the analysis has $\delta p = p_\mathrm{ops} - \left(\frac{mg}{A_\mathrm{eff}} + p_\mathrm{cte} + p_\mathrm{vac} + p_\mathrm{head}\right)$. The 'variable' part $p_\mathrm{head} = \rho g \Delta z$ of the generated pressure occurs because, relative to the laser barometer, the hydrostatic head changes as the cylinder falls down the piston. (For room-temperature argon and cylinder displacement $\Delta z = 6$ mm, $p_\mathrm{head} \approx 1.0$ μPa Pa^{-1}—a significant disturbance compared to the x-axis result.) The 'fluctuating' part p_vac of the generated pressure is what is happening inside the bell jar, and this was measured with a vacuum gage. (The bell jar vacuum slowly fluctuates (0.2 ± 0.1) Pa about its average, equivalent to 0.2 μPa Pa^{-1}.) The 'temperature' part $p_\mathrm{cte} \approx -2\alpha_\mathrm{WC}(t_{90} - 20)p$ of the generated pressure compensates for thermal expansion of the artifact caused by changes in temperature during the fall—the resolution of this compensation is no better than 0.1 μPa Pa^{-1}. The 'constant' part $\frac{mg}{A_\mathrm{eff}}$ of the generated pressure has $A_\mathrm{eff} = A_0(1 + b\Delta p)$;

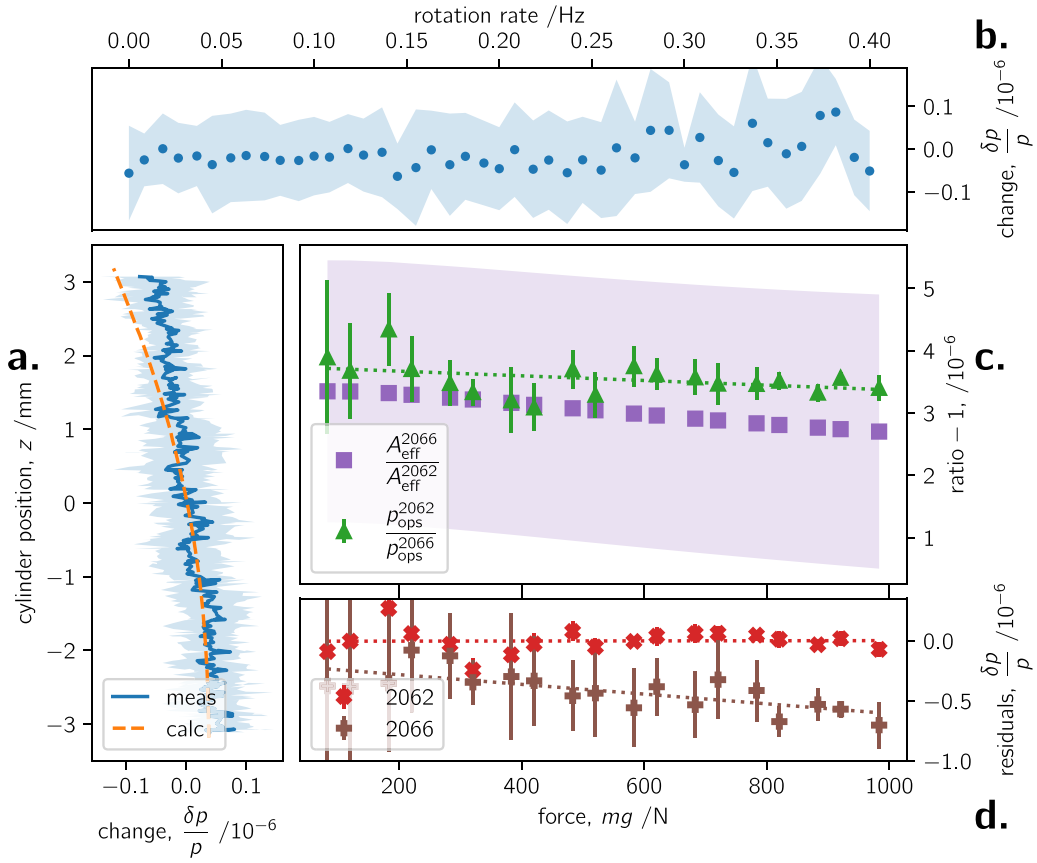

Figure 4. Performance tests with a laser barometer. (a) The change in generated pressure as the cylinder falls down the piston. (b) The change in generated pressure as a function of the cylinder rotation rate. (c) Ratios of optical pressures compared to ratios of calculated areas. (d) Residuals from equation (11) using the coefficients $\mathcal{A}$, $\mathcal{B}$, and $\mathcal{C}$ tied to $p_{\rm mpg}^{2062}$. In (a) and (b), the opaque points are the average of ten repeats, and the shaded area spans the standard deviation. In (c), the shaded area on $A_{\rm eff}^{2066}/A_{\rm eff}^{2062}$ spans the standard uncertainty for the calculation (see text). In (c) and (d), the errorbars on $p_{\rm ops}^{2062}/p_{\rm ops}^{2066}$ and δp span the standard deviation for five repeats.

therefore, it incorrectly assumes A_0 and b have no dependence on z. This assumption causes an error $\delta A_{\rm eff} = [A_0(z) - A_0(0)] + \Delta p[A_0(z)b(z) - A_0(0)b(0)]$. For PCA2062, the first term $A_0(z) - A_0(0)$ fractionally increases $A_{\rm eff}$ by 2.5×10^{-8} as the cylinder falls from $z = 3$ mm to $z = -3$ mm, while the second term $\Delta p[A_0(z)b(z) - A_0(0)b(0)]$ dominates at $\Delta p =$ 469 kPa, and fractionally decreases $A_{\rm eff}$ by 1.6×10^{-7}.

The net result for PCA2062 is that the 'constant' part of the generated pressure is predicted to change by about 0.14 μPa $\rm Pa^{-1}$ for the 6 mm of cylinder displacement—a small effect. The calculated effect on $p_{\rm mpg}$ for the combined z-dependence of A_0 and b is shown as the dashed line in figure 4(a). The measured error $\delta p = p_{\rm ops} - p_{\rm mpg}$ closely follows the calculation, offering good evidence that the laser barometer has corroborated this aspect of the piston gage model.

4.2. Effect of rotation rate

A second test used the laser barometer to monitor changes in generated pressure as the rotation rate of the cylinder naturally decelerated [29] to a stop. This test was performed in absolute mode, operating at 195 kPa with the bell jar pumped to $p_{\rm vac} < 0.3$ Pa. (From table 3, at 195 kPa the time-constant for rotational decay is about 1.1 h.)

The result is shown in figure 4(b) for the artifact PCA2062, where the rotation rate has been discretized by the resolution of the tachometer that is internal to the piston gage system. As above, the analysis has $\delta p = p_{\rm ops} - \left(\frac{mg}{A_{\rm eff}} + p_{\rm cte} + p_{\rm vac} + p_{\rm head} + p_{\rm fall}\right)$, but with the additional 'falling' part $p_{\rm fall} = -1.8 \times 10^{-8} \cdot p\Delta z$ of the generated pressure, which compensates for axial displacement of the cylinder relative to the fixed piston. Based on figure 4(b), for any non-zero rotation, there is no evidence that the generated pressure has a dependence on the rotation rate that is greater than 0.1 μPa $\rm Pa^{-1}$. Indeed, the data support an interpretation that the generated pressure does not significantly change at zero rotation. As aforementioned, the Poiseuille flow coefficient used to calculate the effective area has non-slip boundaries, which is not a complete model for the rotating cylinder. The test in figure 4(b) suggests that the effect of rotation on flow should not change the calculated area by more than $10^{-7} \cdot A_{\rm eff}^{2062}$. Nevertheless, a theoretical estimate of this effect remains absent from the piston gage model.

It is mentioned that the test in figure 4(b) was only practicable with PCA2062. The other cylinders in this set hug the piston at zero rotation, and do not float and generate pressure. Furthermore, when rotating, the other cylinders sinusoidally displace up and down the piston, with a peak-to-peak amplitude of ±0.12 mm and period of 330 s, independent of operating pressure. Comparisons against the laser barometer confirmed that this cylinder displacement corresponds to periodic pressure oscillations of about ±0.4 μPa Pa^{-1}, which is 20 times larger than the head effect. This noisy pressure of the other PCA will be problematic in the test below. Clearly, the test in figure 4(b) is not the final word on the effect of rotation on the generated pressure, and should be taken as the best-case scenario. The artifact PCA2062 is considered anomalously good: it has out-of-roundness that is two times smaller than the other PCAs.

4.3. Optical crossfloat

Finally, a third test used the laser barometer to measure optical pressure ratios between two different PCAs. With the same mass–force applied, each PCA generates a different pressure, because their areas differ. When connected to the laser barometer, each PCA 'generates' two different gas refractivities, which are best converted to a respective p_{ops} (to account for small differences in gas temperature). To take the artifacts PCA2062 and PCA2066 as an example: the ratio $p_{\mathrm{ops}}^{2062}/p_{\mathrm{ops}}^{2066}$, measured with the same mass–force applied to the respective assembly, becomes a proxy for $A_{\mathrm{eff}}^{2066}/A_{\mathrm{eff}}^{2062}$. Effectively, the approach is crossfloat by laser barometry. [The notation $p_{\mathrm{ops}}^{206x} \equiv p_{\mathrm{ops}} - (p_{\mathrm{mass}} + p_{\mathrm{cte}} + p_{\mathrm{vac}} + p_{\mathrm{head}} + p_{\mathrm{fall}})$ means the measured optical pressure has been adjusted to constant PCA conditions. This adjustment ensures that the measured quantity $p_{\mathrm{ops}}^{206x} \to F/A_{\mathrm{eff}}^{206x}$ is governed only by the effective area and distortion coefficient; force F is constant. Adjustments comprise: differing cylinder masses, thermal expansion, bell jar pressure, head height, and cylinder position.]

The test was performed in argon. Therefore, the area of PCA2062 stated in section 2 for helium, should be updated for the different species

$$A_{\mathrm{eff}}^{2062} = 1961.0293\,(37)\left[1 + 6.37\,(73) \times 10^{-12}\,\frac{\Delta p}{\mathrm{Pa}}\right]\ \mathrm{mm}^2,$$

and the area of PCA2066 should be established in argon using the calculation methods in section 2:

$$A_{\mathrm{eff}}^{2066} = 1961.0360\,(55)\left[1 + 4.89\,(94) \times 10^{-12}\,\frac{\Delta p}{\mathrm{Pa}}\right]\ \mathrm{mm}^2.$$

Therefore, in argon at 20 °C and absolute mode, the calculated area ratio is $A_{\mathrm{eff}}^{2066}/A_{\mathrm{eff}}^{2062} = 1.0000034(21)[1 - 1.5(13) \times 10^{-12}\,\frac{\Delta p}{\mathrm{Pa}}]$. From table 1, for the uncertainty of a calculated ratio, only the entries $\mathcal{E}$, flow, and b contribute; all the PCAs were dimensioned in the same setup [6] so that the systematic error in D would be common. The stated uncertainty in the calculated ratio is dominated by the characteristics of PCA2066. Compared to PCA2062, the components $\mathcal{E}$, flow, and b for PCA2066 are larger by factors of 2.1, 2.3, and 1.4, respectively.

To deduce the *absolute* optical pressures, something fundamental must be said about the properties of argon gas, and how the measured refractivity at a known temperature is converted to pressure [37]. Here, instead, the analysis proceeds as *relative*. The pressure generated by PCA2062 was treated as the reference, and the isothermal ($t_{90} \approx 20$ °C) refractivity measurements were fitted

$$p_{\mathrm{mpg}}^{2062} \to p_{\mathrm{ops}}^{2062} = (n-1)\,\mathcal{A}T\left[1 + (n-1)\,\mathcal{B} + (n-1)^2\,\mathcal{C}\right], \tag{11}$$

with $\mathcal{A} = \frac{2R}{3A_{\mathrm{R}}}$. This first step tied the optical and thermophysical properties of argon gas (i.e., the proportionality coefficients $\mathcal{A}$, $\mathcal{B}$, and $\mathcal{C}$) to the diameter of PCA2062, so that $p_{\mathrm{ops}}^{2062} \equiv p_{\mathrm{mpg}}^{2062}$ in the least-squares sense. Then, without further adjustment to the proportionality coefficients, the refractivity and temperature data from the PCA2066 isotherm were processed with the right-hand side of equation (11) to obtain p_{ops}^{2066}. This ratiometric (relative) analysis produces the desired $p_{\mathrm{ops}}^{2062}/p_{\mathrm{ops}}^{2066}$, and it also offers some insight into non-linearity, as explained below. (The measurements reported here are so precise that the temperature dependence of $\mathcal{B}$ and $\mathcal{C}$ in equation (11) should be included, even for the few millikelvin fluctuation on the isotherm. Details on these dependencies are given in [37].)

The ratios $A_{\mathrm{eff}}^{2066}/A_{\mathrm{eff}}^{2062}$ and $p_{\mathrm{ops}}^{2062}/p_{\mathrm{ops}}^{2066}$ are plotted in figure 4(c), which shows excellent agreement. The average difference is 0.5 μPa Pa^{-1}. At zero force, the area ratios are independent of the distortion coefficient b, and the difference is within 0.3 μPa Pa^{-1}. The result of figure 4(c) greatly increases confidence in the piston gage model and area calculation: it is independent confirmation that the ratios of calculated areas are equivalent to the ratios of measured pressures within 0.3 μPa Pa^{-1}. Some experimental details are mentioned. In these crossfloat tests, each of the 19 set pressures were repeated five times. A repeat measurement entailed a pumpout to high-vacuum and a refill with pure argon (and refloating of the PCA). A fully-automated 95-point isotherm took 85 h to acquire. The switch between PCA2062 and PCA2066 broke the pure gas volume, but an overnight pumpout removed all contaminants before the second isotherm was acquired.

An alternate analysis of the optical crossfloat obviates the adjustment to $F/A_{\mathrm{eff}}^{206x}$, but its interpretation is less clear. The alternate analysis adds an offset to equation (11), and $\mathcal{A}$, $\mathcal{B}$, and $\mathcal{C}$ are free parameters when *both* PCA datasets are regressed. A pressure offset term in equation (11) is justified, such as might arise from mass error in the piston gage, or glass temperature error (cavity expansivity) in the laser barometer. The analysis seeks the ratio $(\mathcal{A}^{2062}/\mathcal{A}^{2066})_T$ as proxy for $A_{\mathrm{eff}}^{2066}/A_{\mathrm{eff}}^{2062}$, and the optical measurements (fit coefficients) are adjusted to isothermal argon (constant and same temperature in both runs). Effectively, the analysis uses single-isotherm refractive-index gas thermometry [5] as the consistency check in pressures generated with two different PCAs. The disagreement between isothermal $(\mathcal{A}^{2062}/\mathcal{A}^{2066})_T$ and the calculated area

ratio $A_{\mathrm{eff}}^{2066}/A_{\mathrm{eff}}^{2062}$ was within 0.7×10^{-6}. While this analysis bounds combined inconsistency in A_0 and b, a full understanding is veiled by fitting effects in gas thermometry. For example, the non-linear terms in equation (11) would be best identified by multi-isotherm regression, and an argument can be made that the ratio $(\mathcal{A}^{2062}/\mathcal{A}^{2066})_T$ should be produced with fixed $\mathcal{B}$ and $\mathcal{C}$ (i.e., it is the same gas at the same temperature). If the analysis is performed with $\mathcal{B}$ and $\mathcal{C}$ being the (fixed) average value of both PCA datasets, and leaving $\mathcal{A}$ and the offset as free parameters, disagreement between the measured (fit) and calculated ratios reduces to 0.2×10^{-6}. Further discussion on fitting effects in gas thermometry is outside the scope of the present article, and these sub-$10^{-6}\cdot p$ difficulties comparing mechanical and optical ratios are set aside. Next, some useful information is obtained by looking at the residuals.

The residuals plotted in figure 4(d) have $\delta p = p_{\mathrm{ops}} - p_{\mathrm{mpg}}$. From above, $p_{\mathrm{ops}}^{2062} \equiv p_{\mathrm{mpg}}^{2062}$ in the least-squares sense; therefore, a linear fit to δp^{2062} has a mean and slope of approximately zero. However, three pieces of quasi-independent information can be unraveled from the residuals:

(i) The non-zero mean of δp^{2066} is synonymous with $A_{\mathrm{eff}}^{2066}/A_{\mathrm{eff}}^{2062} - p_{\mathrm{ops}}^{2062}/p_{\mathrm{ops}}^{2066} \neq 0$ from figure 4(c) and above; the y-axis intercept has $\delta p^{2066} = -0.2$ μPa Pa^{-1}. This non-zero intercept is caused by the combined effects of error in the dimensioning, error in the piston gage model, and irreproducibility of the laser barometer (refractometer plus thermometer). It is difficult to conceive irreproducibility in the (untouched) laser barometer exceeding 0.2 μPa Pa^{-1} across the eight-day duration of the two optical crossfloats. Consequently, δp^{2066} is interpreted as confirmation that the piston gage model (i.e., the conversion of diameter to generated pressure) is consistent within 0.4 μPa Pa^{-1}, and that the dimensional characterization is consistent within 10 nm. (To be clear, this does not mean that diameters are known within 10 nm; rather, the statistical error in the dimensional characterization is less than 10 nm.)

(ii) The non-zero slope on δp^{2066} is caused by the combined effect of error in the piston gage flow model plus error in the calculation of the distortion coefficient. As above, it is difficult to conceive compressibility of the laser barometer changing during the eight-day (isothermal) test; this assumption is largely confirmed by the δp^{2062} residuals. The 4.1×10^{-10} N^{-1} slope on δp^{2066} means that the error in the distortion coefficient b, calculated for a single PCA, might be as large as $\frac{1}{\sqrt{2}}8.8\times10^{-13}$ Pa^{-1}, or 12.4 %. The result is somewhat surprising. On the one hand, it is within the allowable mutual standard uncertainty of 24 % in b for PCA2062 and PCA2066; on the other hand, this failure to accurately predict b is of significance to gages operating at $p > 1$ MPa. (To be clear, the slope on δp^{2066} does not mean all the distortion error is in the calculation of b^{2066}; the more correct interpretation is that the error in the calculation of b^{2062} has been written into the properties of argon gas in the initialization of equation (11).)

(iii) Little about both sets of residuals δp^{2062} and δp^{2066} suggests non-linearity. The larger residuals δp^{2066} can be attributed to the ±0.4 μPa Pa^{-1} oscillating pressure of PCA2066 as it rotates; the magnitude of these residuals conforms with the entry $\mathcal{G}$ in table 1. For δp^{2062}, the standard deviation in the residuals is less than 0.2 μPa Pa^{-1}—a remarkable result. Even if the hint of non-linearity in figure 4(d) were real, it is unclear to which instrument the non-linearity should be attributed. (An imprint of non-linearity might appear from statistically imperfect application of equation (11), for example.) For the refractometer, it is difficult to imagine non-linearity in a monolithic homogeneous block of glass suspended by cables. At these low pressures, non-linearity in elastic properties [38] is negligible. Similarly, at these gas densities, the higher-order terms truncated from equation (11) are below 0.1 μPa Pa^{-1}. Also, [39] presented good evidence that two intercompared refractometers are linear within 0.1 μPa Pa^{-1} for pressures up to 180 kPa. These three considerations vouch that non-linearity in δp should not be attributed to p_{ops}. However, the refractometer is not absolved because this single-cavity configuration has offset errors of about 30 mPa, which would explain some of the low-pressure structure. Moreover, unexpected behavior has been observed in a similar homogeneous refractometer by Yang *et al* [40], some 150 times larger than the structure in figure 4(d) (see their figure 14). For the piston gage, rarefied gas dynamics and the calculation methods of section 2 predict no non-linearity greater than ±0.04 μPa Pa^{-1}; see figure 3(b). However, the piston is clamped in an inhomogeneous assembly, and the cylinder is monolithically inhomogeneous—it is made with an epoxy joint between the tungsten carbide cylinder and titanium cup. In principle, these inhomogeneities may give rise to non-linearity as a function of pressure that would be lost by an idealized model; however, it would instinctively seem that the very high elastic modulus of tungsten carbide should ensure the distortion coefficient b is immune to mismatch effects. Therefore, the present work comes to no firm conclusion about non-linearity in a piston gage or a laser barometer; however, figure 4(d) attests that any non-linearity would be very small.

4.4. Summary of the laser barometer tests

The tests reported in this closing section have validated several aspects of the area calculation outlined in section 2. The success of these tests adds confidence that the piston gage model is a reliable physical description of the artifact standard, within the uncertainty stated in table 1. The findings of the tests are:

- The pressure generated by the piston gage changes as the piston falls down the cylinder. Optical measurements agree with calculation within 0.1 μPa Pa^{-1}.
- An experimental estimate has been placed on how much error may arise by the fact that rotation is not accounted for in the flow model. Tests that monitored the generated pressure as the cylinder decelerated to a stop suggest that this

error is no larger than 0.1 μPa Pa^{-1} in PCA2062, an artifact of unusually good form. This experimental estimate lacks theoretical confirmation.

- An optical crossfloat produced a ratio of two measured pressures, generated by two respective PCAs. The ratio of the measured pressures agreed with the ratio of calculated areas within 0.3 μPa Pa^{-1}. Additionally, when generated pressures from the two PCAs are compared to the optical pressure scale, the trend (slope) in disagreement confirms that the error in the calculated distortion coefficient b is no larger than 12.4 %.
- Any hint of non-linearity in either the piston gage or laser barometer is no larger than 0.2 μPa Pa^{-1} for PCA2062. The present tests have not identified the more non-linear instrument. It must be stated that, if real and attributable to the piston gage, non-linearity would be an order of magnitude smaller than the combined uncertainty stated in table 1.

5. Conclusion

A procedure has been described to convert a dimensional dataset to an effective area for a PCA. The procedure first fuses together all dimensional inputs (diameter, straightness, and roundness) to form the birdcage and average generatrix. The flow (distributed pressure) down the gap between the piston and cylinder is then calculated using the theory of rarefied gas dynamics. Next, the distributed pressure is parameterized to load a finite element model, which estimates the geometric distortion to the generatrices. Finally, the calculation is iterated to convergence. The entire procedure runs in a self-contained script, which executes the finite element program as a function call.

Based on the quality of the dimensional characterization, its reproducibility, and a detailed error analysis, it seems realistic that the artifact PCA2062 can approach 2 μPa Pa^{-1} standard uncertainty. From an optimistic viewpoint, this work has reported some ratio and relative tests against a laser barometer, which suggest that the reproducibility, precision, and linearity of the artifact standard are an order of magnitude smaller than this uncertainty estimate. The counterpoint recalls that the authoritative work of Schmidt *et al* [16] claimed $3.0 \times 10^{-6} \cdot p$ uncertainty in the 36 mm diameter PCA39. When scaled for differences in diameter, the work of Schmidt *et al* translates to $2.2 \times 10^{-6} \cdot p$ for the 50 mm diameter PCA2062. The pessimistic view holds that despite a generation of progress in dimensional metrology and flow modeling, the performance of the (other) last artifact-based standard [2] remains essentially unchanged. Indeed, if anything, recent evidence in key comparisons of diameter [41, 42], urge caution below the 4 μPa Pa^{-1} level (100 nm in diameter). Crossfloat comparisons that show agreement between force and diameter ratios at fractionally within 10^{-6} may lead to false-confidence: ratios validate the consistency of the dimensional characterization, not its accuracy. A stringent test is desired between the optical and mechanical pressure scales at the level of a few $10^{-6} \cdot p$.

Acknowledgments

This work was greatly assisted by Fluke Calibration, who hosted one of the authors (PFE) for a workshop in Phoenix AZ in April 2019. Robert Haines and Michael Bair at Fluke Calibration provided essential guidance in the operation of a state-of-the-art piston gage.

Initial work on the area/flow of PCA2062 was undertaken in the second-half of 2015 by Felix Sharipov from the Universidade Federal do Paraná, Curitiba, and Yuanchao Yang from the National Institute of Metrology, Beijing. Their working-report 'Effective cross section of piston–cylinder gages,' dated 27 January 2016, was the starting-point for section 2 in this article.

Appendix. Supplementary information

The supplementary material to this article is available at the NIST data repository https://doi.org/10.18434/mds2-2698. The supplementary material is an archive file, containing the dimensional dataset of PCA2062 and the conversion scripts.

- The main Python script is `CalcAeff2062.py`. This script controls the area conversion process, and runs standalone. It has two dependencies. First, it calls `findGcyl2062.py` and `findGpis2062.py`. These two scripts load the dimensional datasets and find the best-fit generatrices of the piston and cylinder. The second dependency is that a finite element program is required to calculate distortion. The present implementation uses Ansys [43]. The main script `CalcAeff2062.py` dynamically updates the finite element scripts for the applied pressure load distributed down the gap, and runs Ansys as a function call.
- The dimensional datasets of the PCA2062 are included. The dimensional characterization was undertaken in Fall 2020. The dataset comprises straightness and roundness traces, and two-point diameters.

ORCID iDs

Patrick F Egan https://orcid.org/0000-0003-2403-3950
John R Stoup https://orcid.org/0000-0003-3189-0889
Christopher W Meyer https://orcid.org/0000-0001-9124-3339

References

[1] Jousten K 2019 A unit for nothing *Nat. Phys.* **15** 618
[2] Phillips W D 2019 The end of artefacts *Nat. Phys.* **15** 518
[3] Molinar G F *et al* 1999 CCM key comparison in the pressure range 0.05 MPa to 1 MPa (gas medium, gauge mode). Phase A1: dimensional measurements and calculation of effective area *Metrologia* **36** 657–62
[4] Perkin M *et al* 1998 Comparison of pressure standards in the range 10 kPa to 140 kPa *Metrologia* **35** 161–73
[5] Rourke P M C 2021 Perspective on the refractive-index gas metrology data landscape *J. Phys. Chem. Ref. Data* **50** 033104

[6] Stoup J, Ren W, Stanfield E and Egan P Piston-sleeve diameter characterization at NIST *Metrologia* (in preparation)

[7] Sabuga W, Sharipov F and Priruenrom T 2011 Determination of the effective area of piston–cylinder assemblies using a rarefied gas flow model *PTB-Mitteilungen* **121** 260–2

[8] Sabuga W and Priruenrom T 2007 An approach to the evaluation of dimensional measurements on pressure-measuring piston-cylinder assemblies *Proc. Joint Int. Conf. IMEKO TC3/TC16/TC22*

[9] Dadson R S, Lewis S L and Peggs G N 1982 *The Pressure Balance: Theory and Practice* (Her Majesty's Stationery Office)

[10] Sharipov F 2016 *Rarefied Gas Dynamics: Fundamentals for Research and Practice* (Wiley) (https://doi.org/10.1002/9783527685523)

[11] Dadson R S, Greig R G P and Horner A 1965 Developments in the accurate measurement of high pressures *Metrologia* **1** 55–67

[12] Bass A H 1978 Analysis of mechanical pressure generators *J. Phys. E: Sci. Instrum.* **11** 682–8

[13] Sharipov F 2002 Application of the Cercignani–Lampis scattering kernel to calculations of rarefied gas flows. I. Plane flow between two parallel plates *Eur. J. Mech.* B **21** 113–23

[14] Lo S S, Loyalka S K and Storvick T S 1983 Rarefied gas flow in a cylindrical annulus *J. Vac. Sci. Technol.* A **1** 1539–48

[15] Jain K, Bowers W and Schmidt J W 2003 A primary dead-weight tester for pressures (0.05–1.0) MPa *J. Res. Natl Inst. Stand. Technol.* **108** 135–45

[16] Schmidt J W, Jain K, Miiller A P, Bowers W J and Olson D A 2006 Primary pressure standards based on dimensionally characterized piston/cylinder assemblies *Metrologia* **43** 53–59

[17] Stanfield E, Stoup J, Braine M and Doiron T 2020 Sphere diameter interferometry with nanometer uncertainty *Metrologia* **57** 025003

[18] Stoup J and Doiron T 2021 A novel high accuracy micrometer for the measurement of diameter *Metrologia* **58** 025002

[19] Sutton C M and Fitzgerald M P 2009 Performance aspects of gas-operated pressure balances as pressure standards *Metrologia* **46** 655–60

[20] Sabuga W 2011 Pressure measurements in gas media up to 7.5 MPa for the Boltzmann constant redetermination *PTB-Mitteilungen* **121** 247–55

[21] Sharipov F, Yang Y, Ricker J E and Hendricks J H 2016 Primary pressure standard based on piston-cylinder assemblies. Calculation of effective cross sectional area based on rarefied gas dynamics *Metrologia* **53** 1177–84

[22] Sharipov F and Seleznev V 1998 Data on internal rarefied gas flows *J. Phys. Chem. Ref. Data* **27** 657–706

[23] Schaaf S A 1969 Rarefied gas dynamics *Modern Developments in Gas Dynamics* (Springer) ch 6, pp 235–54

[24] Sharipov F 2011 Data on the velocity slip and temperature jump on a gas-solid interface *J. Phys. Chem. Ref. Data* **40** 023101

[25] Agrawal A and Prabhu S V 2008 Survey on measurement of tangential momentum accommodation coefficient *J. Vac. Sci. Technol.* A **26** 634–45

[26] Sharipov F and Moldover M R 2016 Energy accommodation coefficient extracted from acoustic resonator experiments *J. Vac. Sci. Technol.* A **34** 061604

[27] Sharipov F M and Seleznev V D 1994 Rarefied gas flow through a long tube at any pressure ratio *J. Vac. Sci. Technol.* A **12** 2933–5

[28] Huber M L, Lemmon E W, Bell I H and McLinden M O 2022 The NIST REFPROP database for highly accurate properties of industrially important fluids *Ind. Eng. Chem. Res.* **61** 15449–72

[29] Schmidt J W, Welch B E and Ehrlich C D 1993 Operational mode and gas species effects on rotational drag in pneumatic dead weight pressure gauges *Meas. Sci. Technol.* **4** 26–34

[30] Caubergh M, Draïsma J, Franx G J, Hek G, Prokert G, Rienstra S and Verhoeven A 2007 Measure under pressure: calibration of pressure measurement *55th European Study Group: Mathematics With Industry*

[31] Marques W Jr, Kremer G M and Sharipov F M 2000 Couette flow with slip and jump boundary conditions *Contin. Mech. Thermodyn.* **12** 379–86

[32] Salama A D, Sabuga W and Ulbig P 2012 Measurement of the elastic constants of pressure balance materials using resonance ultrasound spectroscopy *Measurement* **45** 2472–5

[33] Jabbour Z J and Yaniv S L 2001 The kilogram and measurements of mass and force *J. Res. Natl Inst. Stand. Technol.* **106** 25–46

[34] Bair M 2010 A new primary standard for the realization of pressure from 10 to 500 kPa *Simposio de Metrología* pp 1–9

[35] Šetina J, Sefa M, Erjavec B and Hudoklin D 2013 Measurement and modeling of water-vapor diffusion in elastomers with impact in humidity and vacuum measurements *Int. J. Thermophys.* **34** 412–23

[36] Scherschligt J *et al* 2018 Review article: quantum-based vacuum metrology at the National Institute of Standards and Technology *J. Vac. Sci. Technol.* A **36** 040801

[37] Egan P F and Yang Y 2023 Optical $n(p, T_{90})$ measurement suite 1: He, Ar and N_2 *Int. J. Thermophys.* **44** 181

[38] Kondo K, Iio S and Sawaoka A 1981 Nonlinear pressure dependence of the elastic moduli of fused quartz up to 3 GPa *J. Appl. Phys.* **52** 2826–31

[39] Egan P F, Stone J A, Ricker J E and Hendricks J H 2016 Comparison measurements of low-pressure between a laser refractometer and ultrasonic manometer *Rev. Sci. Instrum.* **87** 053113

[40] Yang Y, Rubin T and Sun J 2021 Characterization of a vacuum pressure standard based on optical refractometry using nitrogen developed at NIM *Vacuum* **194** 110598

[41] Picotto G B 2010 Final report on EUROMET.L-K4: calibration of diameter standards, group 1 *Metrologia* **47** 04003

[42] Bánréti E 2010 Final report on EUROMET.L-K4: calibration of diameter standards, group 2 *Metrologia* **47** 04001

[43] Certain equipment, instruments, software, or materials, commercial or non-commercial, are identified in this paper in order to specify the experimental procedure adequately. Such identification is not intended to imply recommendation or endorsement of any product or service by NIST, nor is it intended to imply that the materials or equipment identified are necessarily the best available for the purpose.